Bulletin of the Seismological Society of America

This copy is for distribution only by
the authors of the article and their institutions
in accordance with the Open Access Policy of the
Seismological Society of America.

For more information see the publications section
of the SSA website at www.seismosoc.org

THE SEISMOLOGICAL SOCIETY OF AMERICA
400 Evelyn Ave., Suite 201
Albany, CA 94706-1375
(510) 525-5474; FAX (510) 525-7204
www.seismosoc.org

Bulletin of the Seismological Society of America, Vol. 107, No. 6, pp. 2859–2872, December 2017, doi: 10.1785/0120170084

Scenario Dependence of Linear Site-Effect Factors for Short-Period Response Spectral Ordinates

by Peter J. Stafford, Adrian Rodriguez-Marek, Benjamin Edwards, Pauline P. Kruiver, and Julian J. Bommer

Abstract Ground-motion models for response spectral ordinates commonly partition site-response effects into linear and nonlinear components. The nonlinear components depend upon the earthquake scenario being considered implicitly through the use of the expected level of excitation at some reference horizon. The linear components are always assumed to be independent of the earthquake scenario. This article presents empirical and numerical evidence as well as a theoretical explanation for why the linear component of site response depends upon the magnitude and distance of the earthquake scenario. Although the impact is most pronounced for small-magnitude scenarios, the finding has significant implications for a number of applications of more general interest including the development of site-response terms within ground-motion models, the estimation of ground-motion variability components ϕ_{S2S} and ϕ_{SS}, the construction of partially nonergodic models for site-specific hazard assessments, and the validity of the convolution approach for computing surface hazard curves from those at a reference horizon, among others. All of these implications are discussed in the present article.

Introduction

Site amplification effects in earthquake ground-motion models for response spectral ordinates are commonly decomposed into linear and nonlinear contributions. The nonlinear effects reflect the modification of the soil properties resulting from the nonlinear hysteretic behavior of the near-surface material when exposed to strong levels of excitation from below. This input excitation is described by predictions of motions that are explicitly a function of the magnitude and distance of the causative event. However, the linear contributions to site response are always considered to be independent of the seismological properties of the causative event.

The objective of the present article is to demonstrate that the assumption that linear site response is independent of magnitude and distance is not valid when one considers short-period response spectral ordinates. There are a number of implications of this finding that affect the representation of ground motions and hazard from larger scenarios, and these are outlined in the current article.

Evidence for scenario dependence of linear site-response effects has previously been reported in the literature (Zhang and Zhao, 2009; Zhao *et al.*, 2009, 2015). However, the cause of this dependence was not clearly understood and reconciling these findings was not the objective of these studies. In the present work, we explicitly recognize that the amplitude of response spectral ordinates at short response periods is not driven by the amplitude of the Fourier spectral ordinates at the corresponding frequencies. As discussed in detail by Bora *et al.* (2016), the response spectrum at short periods primarily reflects the strength of the underlying Fourier spectral amplitudes over a broad range of frequencies. For a generic seismological model for far-field shear waves, the range of frequencies that are most relevant are those between the corner frequency of the source spectrum, at the low end, and the effective corner frequency imposed by the combination of anelastic attenuation and site diminution filters (κ filter), at the high end (Anderson and Hough, 1984). When dealing with linear site response, this range of frequencies is slightly modified to reflect the dominant contributions from resonant effects as well as additional damping in the near-surface materials. The principal point to be made in the present article is that this additional source of damping in the linear site response acts as an additional filter (κ_0 filter) that reduces the bandwidth of the Fourier amplitudes that can contribute to the short-period response spectral ordinates. For large magnitude scenarios, the curtailment of the frequency range by this additional near-surface damping does not have a significant impact because the source corner frequency is relatively low and the short-period response spectral ordinates are dominated by Fourier contributions just above this corner frequency. However, when considering small-magnitude events, the source corner frequency is already relatively high and so the additional damping has a significant impact upon the available bandwidth.

For the large-magnitude events that have historically been of primary interest in engineering seismology, and

for response periods of most common engineering interest (broadly 0.1–2 s), the frequency range in the Fourier domain that contributes most strongly to input reference horizon response spectral amplitudes are also those that contribute most strongly to the surface response spectral amplitudes. The linearity of the site transfer function in the Fourier domain therefore also acts to modify the response spectral ordinates in a linear manner. In contrast, however, the frequency range driving the short-period response spectral ordinates at some deep reference horizon is broader than the range available to contribute to the surface response spectral ordinates. The direct implication of this phenomenon is that the linear site amplification of response spectral ordinates is weaker (and can involve deamplification) for small and nearby events dominated by high frequencies than it is for larger and more distant events.

The following section presents the theoretical background that explains why this scenario dependence of linear site response arises. Following that, we present evidence from real-world studies that corroborate the theoretical predictions. Finally, we discuss a number of implications of these results that affect the development of ground-motion models as well as the undertaking of site-specific seismic hazard analyses.

Theoretical Background

The scaling of response spectral ordinates can be understood by examining the scaling of the zeroth spectral moment (Boore, 2003; Bora *et al.*, 2016). Response spectral ordinates can be shown via random vibration theory (RVT) to be proportional to the square root of the zeroth spectral moment:

$$S_a \propto \sqrt{m_0}. \tag{1}$$

To move from the proportionality to an exact equality, equation (1) needs to be modified to include duration-dependent terms that relate the zeroth moment to the root mean square (rms) amplitude, and an additional duration-dependent term to link the peak oscillator response to the rms response (Boore, 2003).

The zeroth spectral moment is defined as

$$m_0 = 2\int_0^\infty |Y(f, f_n, \zeta_n)|^2 df, \tag{2}$$

in which $Y(f, f_n, \zeta_n)$ is the Fourier spectrum of the response of a single-degree-of-freedom (SDOF) oscillator with a natural frequency of f_n and a damping ratio of ζ_n. The Fourier amplitude spectrum (FAS) itself can be described as the product of the FAS of accelerations appropriate for some reference horizon below the ground surface $A(f)$, the transfer function associated with dynamic response of the material above this horizon $S(f)$, and the transfer function of the SDOF oscillator $H(f, f_n, \zeta_n)$.

A general expression for the FAS of accelerations at some reference horizon can be given as

$$A(f; m, r) = \frac{\mathbb{C} M_0 f^2}{(1 + (f/f_c)^2)} g(r) \exp[-\pi f(\kappa_r + \kappa_0)] I(f) \tag{3}$$

(Brune, 1970; Boore, 2003), in which the exponential filter has contributions that reflect the loss of energy along the travel path as well as a distance-independent component κ_0. The path-dependent contribution is defined as

$$\kappa_r = \frac{r}{Q_0 \beta} \tag{4}$$

when frequency-independent anelastic attenuation is assumed appropriate; $Q_0 \rightarrow Q(f)$, otherwise. The term $I(f)$ reflects the impedance between the source and the reference horizon, $\mathbb{C}$ is a constant term that reflects properties of the source, the orientation of waves leaving the source and arriving at the reference horizon, and the partitioning of energy into orthogonal horizontal components. The frequency-independent function $g(r)$ represents the effects of geometric spreading and would take the form $g(r) = (1/r)^\gamma$ with $\gamma = 1$ for spherical spreading. The source is characterized primarily through the use of the seismic moment M_0 and the source corner frequency f_c, which can itself be expressed as a function of seismic moment and the stress parameter $\Delta\sigma$. The overall function provides a spectrum for a given magnitude and distance, with the magnitude being directly related to the seismic moment.

The most important attribute of the function defining $A(f)$ is that the amplitudes are band limited through the combination of the corner frequency at low frequencies and by the combined effect of the path and site contributions to κ. These latter effects are independent of size of event and will always limit the same range of frequencies at the upper end of the spectrum while the source corner frequency varies significantly with the magnitude of the event and is lower for larger magnitude events.

The transfer function associated with near-surface dynamic response (or site effects) will vary depending upon the particular layering encountered on site. However, for the purposes of exploring the general scaling, consider the simple case of a single homogeneous layer overlying an elastic half-space. When the overlying layer has a thickness H_s, a shear-wave velocity of v_s, density ρ_s, and a damping ratio of ζ_s, the site transfer function in this case can be written as

$$|S(f)| = \left| \frac{1}{\cos\beta^* + i\alpha^* \sin\beta^*} \right| \tag{5}$$

with

$$\beta^* = \frac{2\pi f H_s}{v^*_{s,s}}, \tag{6}$$

and the complex shear-wave velocity is defined as $v^*_{s,s} = v_s(1 + i\zeta_s)$. The complex impedance ratio is then defined as

$$\alpha^* = \frac{\rho_s v^*_{s,s}}{\rho_r v^*_{s,r}}, \tag{7}$$

in which $v^*_{s,r}$ and ρ_r are terms analogous to $v^*_{s,s}$ and ρ_s, but for the underlying medium.

This site transfer function will always exhibit resonant peaks associated with the impedance effects and the layer thicknesses, but will also always exhibit a general decay at high frequencies as well as an asymptotic convergence to unity at very low frequencies.

The overall effect of the site transfer function can therefore be regarded as the combination of resonant effects $|S_r(f)|$ and an exponential filter that is associated with the damping in the near-surface material $S_d(f)$. It can be shown that the site transfer function can be decomposed as

$$|S(f)| = S_d(f)|S_r(f)| \equiv |e^{-i\beta^*}| \left| \frac{1}{1 + \frac{1}{2}(1-\alpha^*)(e^{-i2\beta^*} - 1)} \right|. \tag{8}$$

The first term of this expression is of most interest and can be shown to be equivalent to

$$S_d(f) = |e^{-i\beta^*}| \equiv \exp\left[-\left(\frac{\zeta_s}{1+\zeta_s^2} \right) \frac{\omega H_s}{v_{s,s}} \right] \approx \exp\left[-\frac{\zeta_s \omega H_s}{v_{s,s}} \right] \tag{9}$$

which has the same form as a κ filter. The effect of the material overlying the reference horizon is to therefore introduce a degree of amplification (which varies with frequency according to resonant conditions) as well as an additional κ filter effect. This can be made explicit by writing

$$S_d(f) = \exp\left[-\frac{\zeta_s \omega H_s}{v_{s,s}} \right] \equiv \exp[-\pi \kappa_\zeta f], \tag{10}$$

in which

$$\kappa_\zeta = \frac{2\zeta_s H_s}{v_{s,s}}. \tag{11}$$

The resonant term of the site response is more complicated, but it tends to be a stable plateau at high frequencies. For this single layer case, it can be shown that in the limit as $f \to \infty$, we can define the average level of amplification as:

$$|S_r(f \to \infty)| = \frac{2}{\sqrt{1 + 2\alpha \frac{1+\zeta_s\zeta_r}{1+\zeta_r^2} + \alpha^2 \frac{1+\zeta_s^2}{1+\zeta_r^2}}} \approx \frac{2}{\alpha + 1}, \tag{12}$$

in which the term $\alpha = \rho_s v_{s,s} / \rho_r v_{s,r}$ is the noncomplex impedance ratio and ζ_s and ζ_r are the damping ratios of the overlying layer and the underlying half-space, respectively. The approximation included in equation (12) is strong given that the ratios involving damping ratios are always very close to unity. It is important to note that this asymptotic limit is independent of the depth of the overlying layer.

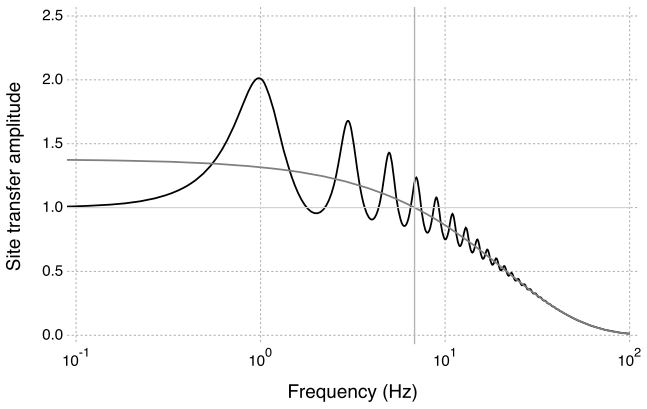

Figure 1. Site transfer function showing the frequency range at which deamplification takes place. The black curve shows the true transfer function while the gray curve shows the generic average scaling corresponding to equation (13). The vertical light-gray line corresponds to f_1 and represents the frequency beyond which deamplification takes place.

Although the specific locations of resonant peaks depend upon this layer thickness, the asymptotic level of amplification at high frequencies does not.

If we are not particularly interested in the resonant effects, or the exact locations of the resonant peaks, we can write a generic expression to reflect the average behavior of the site effects when viewed as a generic filter. This expression is not strictly a mathematical average, but it captures the general scaling of site effects extremely well over the range of high frequencies that are of greatest interest in the present study. This can be appreciated from Figure 1, in which the transfer function for a deep layer ($H_s = 100$ m) of soil with a shear-wave velocity of $v_{s,s} = 400$ m/s, density $\rho_s = 1.8$ t/m^3, and damping ratio $\zeta_s = 0.03$ overlying an elastic half-space with $v_{s,r} = 800$ m/s, $\rho_r = 2.0$ t/m^3, and $\zeta_r = 0.01$ is shown:

$$E[|S(f)|] \approx S_d(f)|S_r(f \to \infty)|. \tag{13}$$

The advantage of developing this generic function is that it permits us to determine the frequency range for which the site response acts to deamplify the input motion in the Fourier domain. This frequency range begins at f_1, defined below, and extends to higher frequencies:

$$f_1 = -\frac{1}{2\pi} \left(\frac{1+\zeta_s^2}{\zeta_s} \right) \frac{v_{s,s}}{H_s} \ln\left(\frac{1}{|S_r(f \to \infty)|} \right). \tag{14}$$

The final component that contributes to the integrand of the zeroth spectral moment calculation is the transfer function for the SDOF oscillator. This function depends upon the natural frequency of the oscillator f_n and its damping ratio ζ_n:

$$|H(f, f_n, \zeta_n)| = \frac{1}{\sqrt{\left(1 - \left(\frac{f}{f_n}\right)^2\right)^2 + \left(\frac{2\zeta_n f}{f_n}\right)^2}}. \tag{15}$$

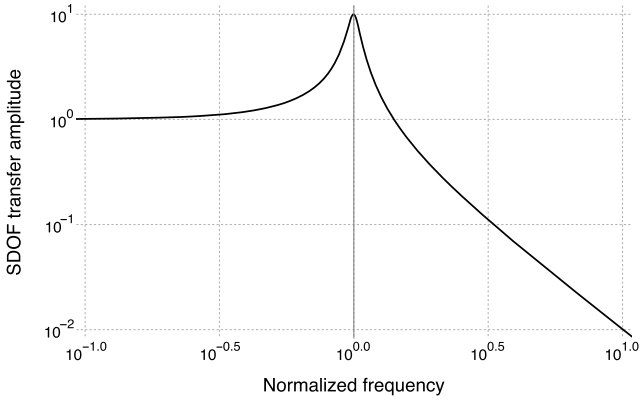

Figure 2. Single degree-of-freedom (SDOF) oscillator transfer function for a damping ratio of $\zeta_n = 0.05$. The horizontal axis shows frequency normalized by the natural frequency of the oscillator f/f_n.

The key feature of this transfer function is that for frequencies well below the natural frequency, the function tends to unity, while for frequencies well above the natural frequency, the transfer function decays as $|H(f \gg f_n, f_n, \zeta_n)| \propto 1/f^2$. At frequencies close to the natural frequency, significant amplification takes place with a value of $1/(2\zeta_n)$ when $f = f_n$. This behavior is shown in Figure 2.

To investigate the modification of response spectral ordinates from some reference horizon to the surface, we can compute

$$\mathrm{Amp}(f_n, \zeta_n) = \sqrt{\frac{m_{0,s}(f_n, \zeta_n)}{m_{0,r}(f_n, \zeta_n)}} \tag{16}$$

with $m_{0,s}(f_n, \zeta_n)$ representing the zeroth moment of the surface spectrum and $m_{0,r}(f_n, \zeta_n)$ being the zeroth moment of the reference horizon spectrum. Here, we are implicitly assuming that the duration dependence that would link the zeroth spectral moment to the spectral amplitude is similar for both the surface and reference horizons. Each of these terms is defined using their constitutive components as

$$\begin{aligned} m_{0,r}(f_n, \zeta_n) &= 2\int_0^\infty |Y_r(f, f_n, \zeta_n)|^2 df \\ &= 2\int_0^\infty |A(f; m, r)|^2 |H(f, f_n, \zeta_n)|^2 df \end{aligned} \tag{17}$$

for the reference horizon and

$$\begin{aligned} m_{0,s}(f_n, \zeta_n) &= 2\int_0^\infty |Y_s(f, f_n, \zeta_n)|^2 df \\ &= 2\int_0^\infty |A(f; m, r)|^2 |S(f)|^2 |H(f, f_n, \zeta_n)|^2 df \end{aligned} \tag{18}$$

for the surface response.

For low oscillator frequencies, particularly when the oscillator natural frequency is below the fundamental site frequency, the moments are relatively similar due to the fact that $S(f) \approx 1$ for frequencies near f_n, and so both integrands behave in a manner similar to $|A(f; m, r)|^2 |H(f, f_n, \zeta_n)|^2$. To demonstrate this effect, we consider a homogeneous soil layer of 100 m thickness, density of 1.8 t/m^3, shear-wave velocity of 400 m/s, and damping ratio of 0.03 overlying an elastic half-space with density of 2.0 t/m^3, shear-wave velocity of 800 m/s, and damping ratio of 0.001. In the upper-left panel of Figure 3, the expected integrands for both the reference horizon and surface motions are shown for a magnitude 6.0 event with a distance of 1 km interacting with this soil profile. The shape of the FAS of the input motions is defined using a single-corner Brune (1970) spectrum with a $\Delta\sigma = 100$ bar stress parameter, pure spherical geometric spreading, a quality factor of $Q = 400$, and κ_0 value in the rock of 0.01. The source shear-wave velocity and density are taken as 3.6 km/s and 2.7 t/m^3, respectively. The integrands in both cases are dominated by the interaction of the Fourier spectrum of the input ground motion as well as the SDOF transfer function (corresponding to an oscillator with 5% of critical damping). The shaded regions shown in this panel demarcate the frequency range corresponding to the accumulation of $\psi(f_{\max}) = 0.05$ and $\psi(f_{\max}) = 0.95$, in which the function $\psi(f_{\max})$ representing the accumulation of spectral moment is defined by

$$\psi(f_{\max}) = \frac{2}{m_0}\int_0^{f_{\max}} |Y(f, f_n, \zeta_n)|^2 df. \tag{19}$$

That is, the lower frequency of this shaded region corresponds to the case where $f_{\max} = f_{\text{lower}}$ and $\psi(f_{\text{lower}}) = 0.05$, while the upper frequency corresponds to the case where $f_{\max} = f_{\text{upper}}$ and $\psi(f_{\text{upper}}) = 0.95$.

The buildup of this accumulated moment is shown in the middle row of Figure 3, in which the value of the upper frequency or $f_{\max}$ is shown on the horizontal axis. In the left of these panels (i.e., for low oscillator frequencies), it can be appreciated from the step-like scaling that the overall spectral moment is dominated by contributions at frequencies very close to the SDOF natural frequency. In the bottom row, a similar plot is shown but where the absolute contributions to the rms response are shown. These contributions to the rms response are represented by $\sqrt{\psi(f_{\max}) m_0}$ with $f_{\max}$ shown on the horizontal axis. The amplitude at which these rms contribution plots become flat represents the final rms amplitude (at least the $\sqrt{m_0}$ component—the actual rms values also require division by the appropriate duration for the considered scenario). As can be seen in the bottom left panel, the rms amplitude for the surface motion is higher than that at the reference horizon, and the ratio of these two values represents the expected degree of amplification for both rms motions and response spectral ordinates with this oscillator frequency.

The behavior seen in the left panels of Figure 3 is also observed for the central panels corresponding to an oscillator frequency of 5 Hz. In this case, the resonant oscillator response still drives the moment integral and the accumulation of the rms and spectral response. However, because the

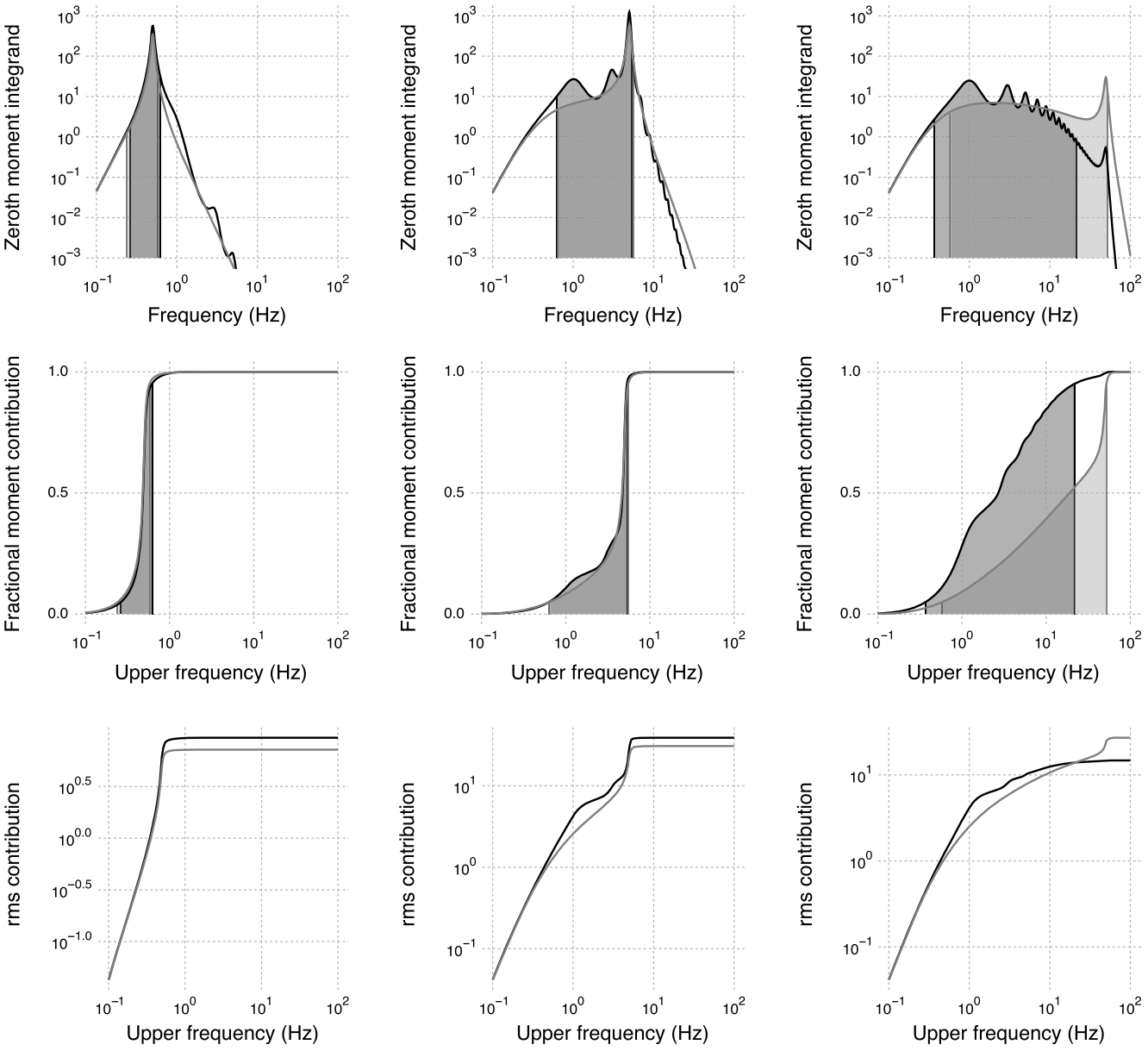

Figure 3. Contributions to response spectral ordinates for a magnitude 6 event at a distance of 1 km. The columns from left to right correspond to natural oscillator frequencies of $f_n = 0.5$, 5.0, and 50.0 Hz, respectively. (Top row) The integrand of the zeroth spectral moment for response spectral ordinates. (Middle row) The fractional contribution to m_0 plotted as a function of the highest frequency $f_{\max}$ used in the integration for m_0. The full moment is recovered as $f_{\max} \to \infty$. (Bottom row) The value of $\sqrt{\psi(f_{\max})m_0}$ plotted against $f_{\max}$. rms, root mean square.

oscillator frequency is now between the source corner frequency and the κ frequency (at which the combined κ filter begins to dominate the Fourier amplitudes) and is also within the range where resonant site effects also play a role, the frequency bandwidth that contributes to the oscillator response has enlarged. However, as can be seen from the central panels of the figure, the main contribution remains concentrated around the oscillator frequency.

For high oscillator frequencies, the effect of the SDOF transfer function on the Fourier spectrum of the reference horizon motions is either to perfectly preserve or to amplify the Fourier spectral ordinates for frequencies below the oscillator frequency. However, what is being preserved in the case that the SDOF transfer function acts on the Fourier spectrum of the surface motions is the combination of the input spectrum and the effects of the site response. Recall that at high frequencies (above f_1), the effect of the site response is to deamplify the input motions. The consequence of this deamplification is seen in the right panels of Figure 3, where now there are very clear differences between the moment integrands for the reference horizon and surface cases. In particular, it can be appreciated that the frequency bandwidths over which moment contributions are made is significantly greater than for the lower frequency cases shown in the left

and central panels. In addition, the relative contribution of the oscillator transfer function and the input motion vary significantly from the reference horizon to the surface response. For the reference horizon case, there is no deamplification effect at frequencies above f_1 (which exists at the surface as a result of the near-surface soil damping). As a result, the resonant peak from the oscillator is still able to make a significant contribution to the spectral moment. In contrast, for the surface response, the additional damping in the near-surface layer causes the input motions to attenuate significantly at high frequencies, to the extent that the amplification associated with the oscillator transfer function provides very little contribution to the overall integral.

This additional near-surface damping leads to the surface rms and spectral amplitudes being smaller than their reference horizon counterparts. Because of the oscillator response, this effect is not necessarily limited to the bandwidth over which deamplification occurs in the FAS. Rather than experiencing site amplification, a significant deamplification in response spectral amplitudes is observed. In all cases discussed herein, the near-surface material is forced to remain linear and this deamplification is taking place under conditions associated with linear site response.

The phenomenon discussed here has initially been presented for a magnitude 6 event in Figure 3. However, the effect is even more significant when considering the response for small-magnitude events—as shown in Figure 4. For the small-magnitude scenarios, the corner frequency is relatively high, and this has implications at both low and high frequencies. In Figure 4, the properties of the soil profile, the SDOF oscillators, and the seismological model are all the same as in Figure 3.

When the oscillator frequency is low and well below the corner frequency of the source spectrum, the scaling of the FAS of ground motions will increase in proportion to f^2. As previously noted, for frequencies well above the oscillator natural frequency, the SDOF transfer function decays in proportion to f^{-2}. Therefore, while the oscillator frequency is below the source corner frequency, the combination of the FAS of the input motions and the SDOF transfer function will lead to a relatively flat Fourier spectrum over the frequency range $[f_n, f_c]$. For frequencies above the source corner frequency, the spectrum will then decay in proportion to f^{-2} or greater. For this reason, the left panels of Figure 4 show a relatively broad range of frequencies contributing to the spectral moment in comparison with the case shown in Figure 3 for the larger magnitude event.

When the oscillator frequency is high, a similar effect is seen as in the large magnitude case, with the exception that now the high source corner frequency dictates that it is not possible for a broad range of frequencies to contribute to the spectral amplitudes. When the near-surface material above the reference horizon is characterized by a degree of damping that is large in comparison with the effects of κ that have influenced the reference horizon motions, there will be a significant difference between the integrands of the zeroth moment at high frequencies. The integrand for the reference horizon will have a significant contribution from frequencies near the oscillator frequency because the damping in the underlying material is relatively low. However, the integrand for the surface response will include the effects of the damping in the near-surface layer and will cause the spectral moment to be dominated by lower frequency contributions. The effect shown in Figure 4 for high oscillator frequencies is a relatively extreme scenario in which the damping in the underlying material ζ_r (related to κ_0 for the reference horizon) is assumed to be relatively low and the contributions from anelastic attenuation are minimal given the short-distance scenario being considered. In the case that a more distant scenario was analyzed, the effect of anelastic losses along the propagation path would result in the integrand of the reference horizon having more effective damping, and the frequencies that were contributing to the spectral moments for the reference horizon and surface cases would be more consistent.

The overall impact of these effects can be demonstrated through comparison of the predicted response spectra for a number of different magnitude and distance scenarios. Figure 5 plots amplitude spectra proportional to the acceleration spectral ordinates for two different distances and five magnitude values. While ordinates are labeled as rms amplitude, the spectra correspond to $\sqrt{m_0}$ for both the reference horizon and the surface response. Any combination of peak factor and duration measure used to convert these ordinates into actual response spectra would have minimal impact on the values of the amplification shown in the bottom panels of the figure. These bottom panels demonstrate that at short periods, below the period corresponding to f_1 and the near-surface damping, there are significant differences in the site-response terms for the different magnitude values at a given distance.

In addition, there is also a clear difference between the nature of the site response at these short periods for the two different distances considered. This distance scaling is the result of the anelastic attenuation playing a stronger role in increasing the effective κ for the reference horizon, which leads to the damping in the near-surface layer having less impact on the frequency band contributing to the spectral response at the two horizons considered.

For both distances, it is also possible to observe some magnitude dependence in the spectral amplification for the longest response periods considered. These differences are the result of the interaction of the source corner frequency with the natural frequency of the SDOF oscillator as discussed previously.

Evidence for Scenario-Dependent Linear Site Effects

Based upon the predictions shown in Figure 5, we should expect to find evidence of these scenario-dependent site effects in short-period response spectral ordinates. One evident consequence of these predictions is that site response

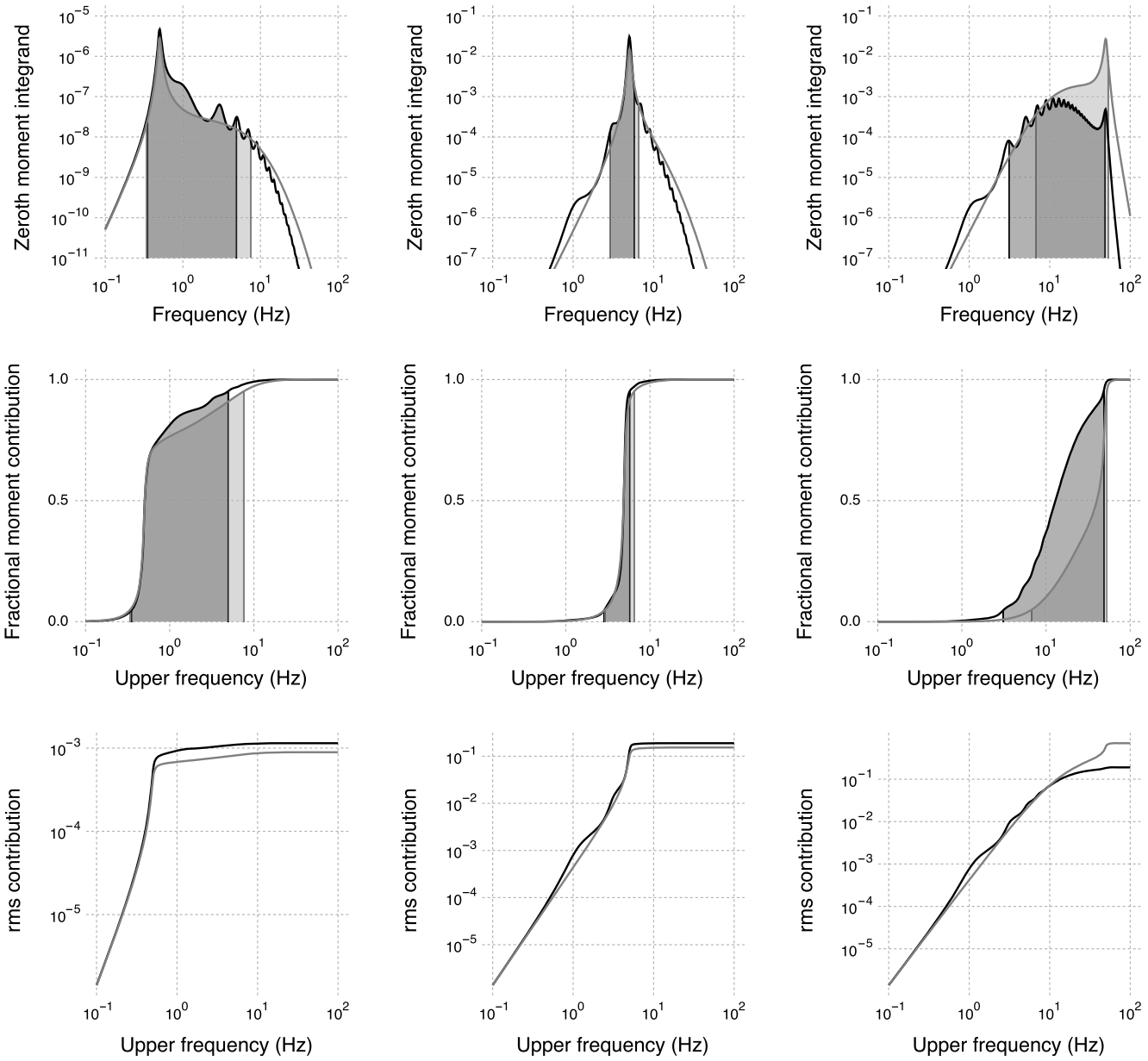

Figure 4. Contributions to response spectral ordinates for a magnitude 3 event at a distance of 1 km. The columns from left to right correspond to natural oscillator frequencies of $f_n = 0.5$, 5.0, and 50.0 Hz, respectively. (Top row) The integrand of the zeroth spectral moment for response spectral ordinates. (Middle row) The fractional contribution to m_0 plotted as a function of the highest frequency $f_{\max}$ used in the integration for m_0. The full moment is recovered as $f_{\max} \to \infty$. (Bottom row) The value of $\sqrt{\psi(f_{\max})m_0}$ plotted against $f_{\max}$.

at sites with significant damping should show magnitude and distance dependence. Empirical evidence of these effects can also be obtained from existing ground-motion records. The present section explores such evidence.

Amplification Functions

We evaluated 1D site response for two soft-soil sites overlying a deep sedimentary column. The sites are underlain by bedrock with a shear-wave velocity of 1400 m/s. These sites are real sites within the Groningen gas field in the northwestern Netherlands where shear-wave velocity measurements were conducted in the upper 30 m, and shear-wave velocities of the deeper layers were estimated using geophysical methods and deep borehole measurements (Kruiver *et al.*, 2017). Mass densities were estimated based on the type of materials in the profile. Small-strain damping ($D_{\min}$) for the deeper layers is assigned using estimates of the quality factor Q to each layer ($D_{\min} = 1/2Q$). Small-strain damping for shallow layers was obtained by scaling laboratory-based measures of small-strain damping (Darendeli, 2001; Menq, 2003) so that they match the estimates of the quality factor Q at nearby borehole arrays. Large values of damping near the surface correspond to near-surface peat

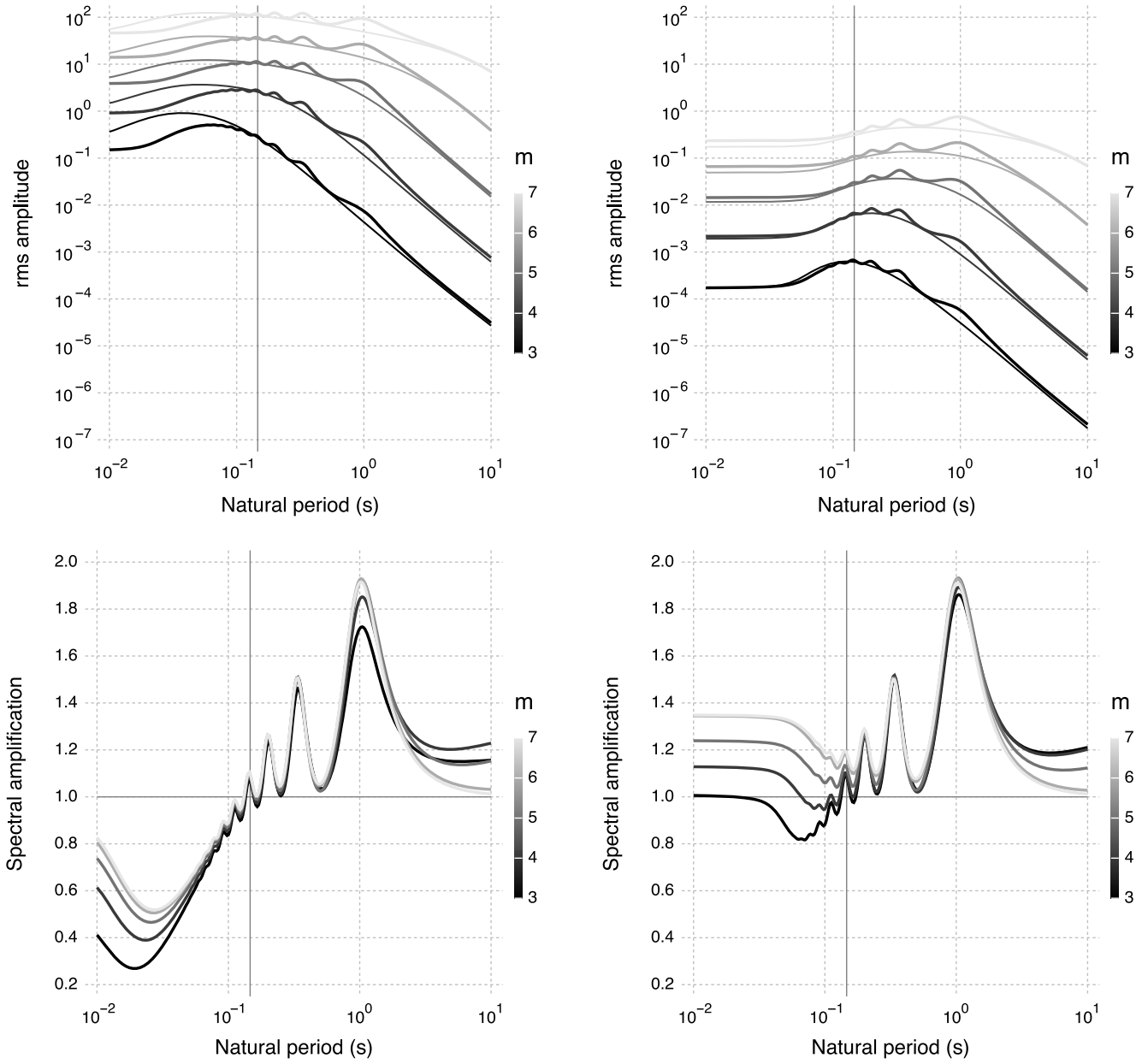

Figure 5. rms amplitude ($\sqrt{m_0}$) spectra in the top panels and spectral amplification factors in the bottom panels all shown against natural oscillator period. The panels on the left show predictions for a distance of 1 km while those on the right show predictions for a distance of 100 km. In the top row, the thin lines represent the spectra at the reference horizon while the thick lines show the surface spectral response.

layers. The shear-wave velocity and damping profile for the two sites are shown in Figure 6. It is noteworthy that the specific details of the shear-wave velocity and damping profiles in Figure 6 are not important, other than the fact that these values are realistic and consistent with the shear-wave velocity and small-strain damping values for a deep soil column. The estimated contribution of material damping from the whole profile to the κ filter (which we term $\Delta\kappa$) can be computed using

$$\Delta\kappa = \int_0^{z_{\text{rock}}} \frac{1}{Q(z)V_S(z)}\,dz \qquad (20)$$

(Hough and Anderson, 1988; Campbell, 2009), in which z_{rock} is the depth to seismic bedrock. The values of $\Delta\kappa$ for the two sites are given in the caption of Figure 6.

Linear elastic 1D site-response analyses were conducted using the software Strata (Kottke and Rathje, 2008), with the RVT option. Input motions, prescribed in terms of FAS, were applied at the bedrock interface (V_S = 1400 m/s, see Fig. 6). The FAS were computed using a point-source seismological model (Boore, 2003). The parameters for the model, including those of the duration model used in the RVT simulations, are discussed in Bommer *et al.* (2017). The value of the site-diminution parameter κ_0 at bedrock is 0.015 s, which is con-

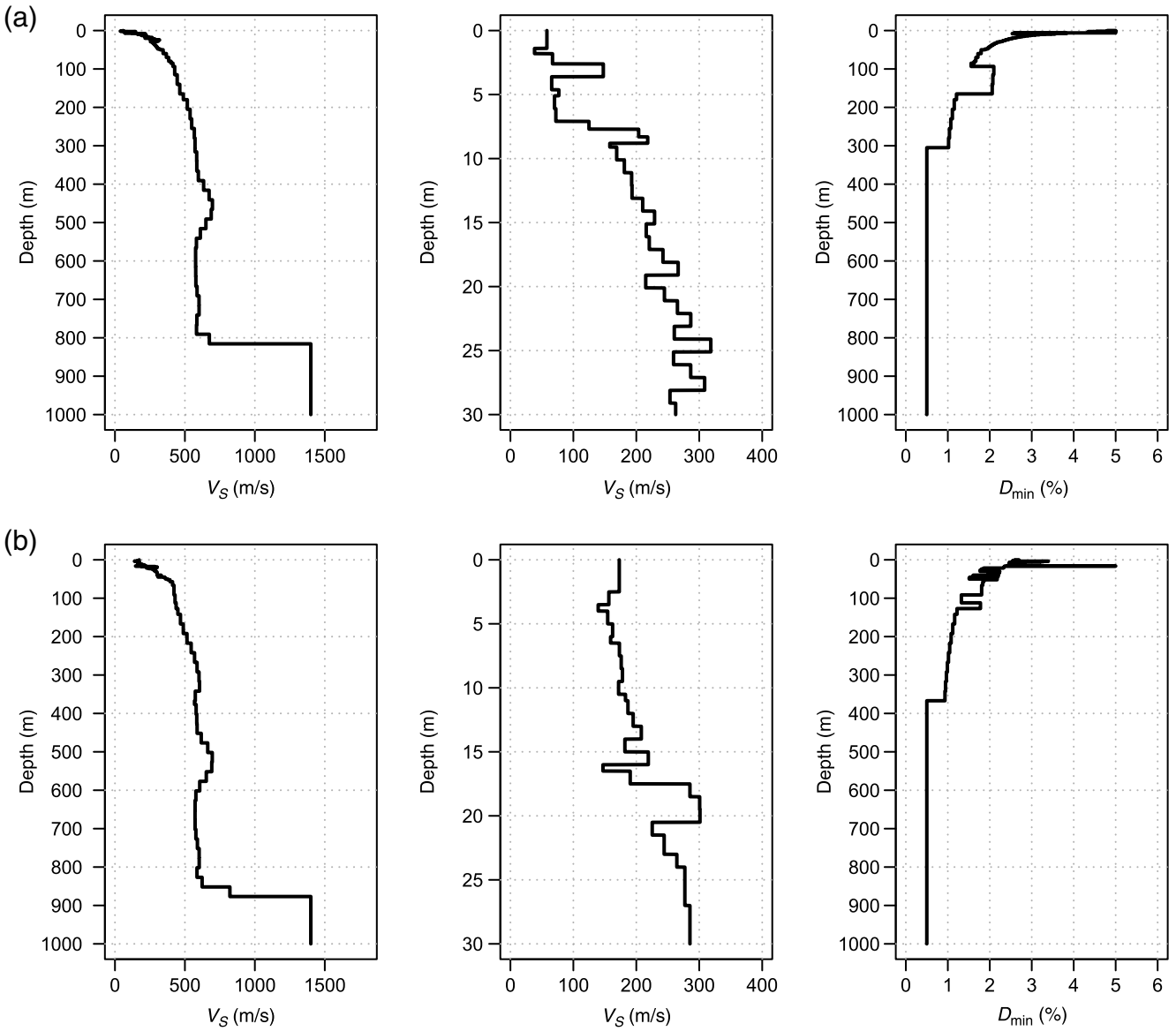

Figure 6. Shear-wave velocity and damping profiles for the two sites considered in this study. Each subplot shows, from left to right, the full V_S profile to bedrock, the V_S profile for the top 30 m, and the damping profile down to bedrock; (a) site 1: $V_{S30} = 138$ m/s and $\Delta\kappa = 0.042$ s; and (b) site 2: $V_{S30} = 200$ m/s and $\Delta\kappa = 0.036$ s.

sistent with the hard-rock conditions for the bedrock interface. The sources are all located at a depth of 3 km. The FAS were generated for a suite of scenarios ranging from magnitude 2.5 to 6.0 and epicentral distances from 0 to 20 km.

The results of the site-response analyses are shown in Figures 7 and 8, for sites 1 and 2, respectively, in terms of spectral amplification function (surface over outcropping bedrock). Observe that there is a strong magnitude and distance dependence for short periods. This dependence weakens as the oscillator period increases. Also note that the degree of magnitude and distance dependence is different for the two sites, indicating that the site characteristics, and in particular the site κ ($\Delta\kappa$ for the near-surface deposits), will have an impact on the shape of the magnitude and distance dependence of the amplification factors. This effect also explains why the shape of the magnitude scaling observed in small-magnitude empirical data cannot simply be captured using a single value of κ (Boore and Campbell, 2017).

Evidence from Recorded Data

Ground-motion models that have generally been developed for databases spanning large ranges of magnitude have ignored the scenario dependence in the linear site response. As a result, when such models are used to make predictions of ground motions, they have needed to account for the effects of the scenario dependence upon the linear site response elsewhere in the model.

In recent studies, such as those within the Next Generation Attenuation (NGA)-West2 project (Bozorgnia *et al.*

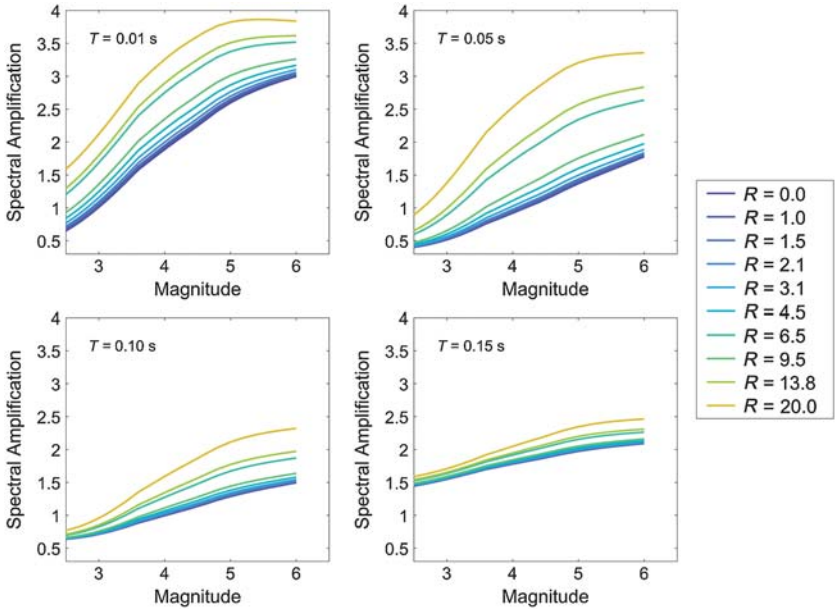

Figure 7. Spectral amplification factors (surface to outcropping bedrock) for site 1 (V_{S30} = 138 m/s and $\Delta\kappa$ = 0.042 s).

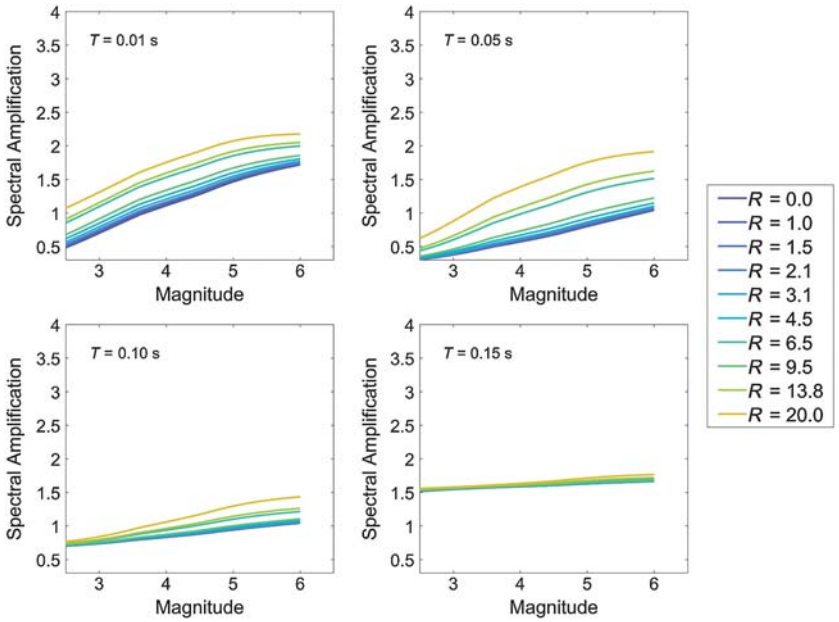

Figure 8. Spectral amplification factors (surface to outcropping bedrock) for site 2 (V_{S30} = 200 m/s and $\Delta\kappa$ = 0.036 s).

2014) or Chiou *et al.* (2010), the magnitude scaling has been modified to include a break from linearity at small magnitudes. These adjustments, or breaks in scaling, reflect the average κ for the database used and relate to the interaction of the source corner frequency and the high-frequency κ filter for small-magnitude events. The result is that this κ effect is viewed as apparent nonlinear magnitude scaling for the small-magnitude events. However, by treating this effect generically as a source-scaling effect, the predictions for a given site with a κ-value that differs from the database average will be biased. In addition, even if the appropriate value of κ for the site was allocated, the approach of representing this kappa effect through magnitude scaling alone will not enable the magnitude and distance dependence of the linear site response to be captured. This is partly the reason why the estimates of variance in small-magnitude data tend to be greater than those for larger events.

The κ effect also has a systematic impact on the estimation of the site-to-site variability ϕ_{S2S}. Because the estimates of ϕ_{S2S} are often based upon the analysis of sites with multiple observations (most likely from small-magnitude recordings), the systematic site effect that is represented within δ_{S2S} includes a component of bias associated with neglecting to account for the magnitude and distance dependence of the linear site response. Figure 9 shows the estimates of ϕ_{S2S} for the KiK-net array in Japan, separately for small magnitude ($M < 5$) and larger magnitude events. These estimates are obtained from the ground-motion prediction equation (GMPE) of Dawood (2014), using KiK-net data (Dawood *et al.*, 2016), considering only the sites with more than 10 recordings. This ground-motion model uses a similar functional form as Abrahamson *et al.* (2014), and hence accounts for a difference in magnitude scaling for small-magnitude events. Observe that, as predicted, the site-to-site variability is larger for small-magnitude events. Moreover, because most of the data used by Dawood (2014) are from small-magnitude events, the overall estimate of site-to-site variability is controlled by the small-magnitude data. The importance of this is clearest when one recognizes that these estimates of site-to-site variability are extrapolated up to be applicable for the larger magnitude events that drive hazard analyses.

Although the average scenario dependence of the site terms (δ_{S2S}) will be partly captured by the magnitude scaling, one would still expect to find a trend with magnitude (and possibly distance) in the within-event residuals at each station, in particular for stations with low values of κ. Figure 10 plots the trends of the within-event residual (δW) versus magnitude for selected stations for an oscillator period of 0.04 s (this period is the period for which the magnitude dependence of residuals is strongest). In these plots, the within-event residual is corrected by the average site term

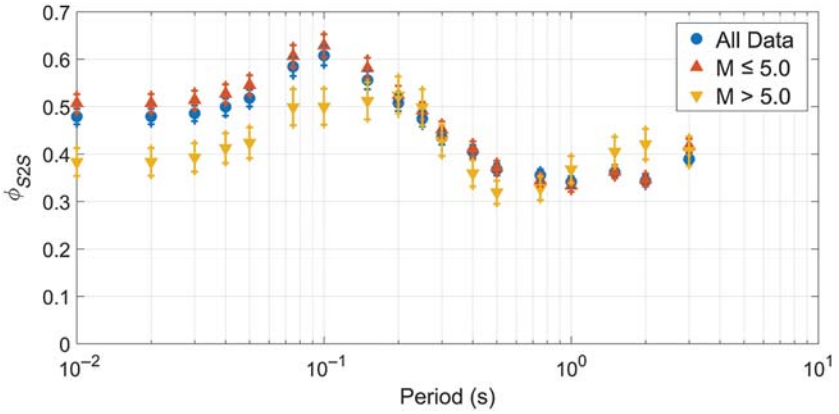

Figure 9. Site-to-site standard deviation (ϕ_{S2S}) for the KiK-net database, considering only stations with at least 10 recordings. The data are shown separately for different magnitude ranges.

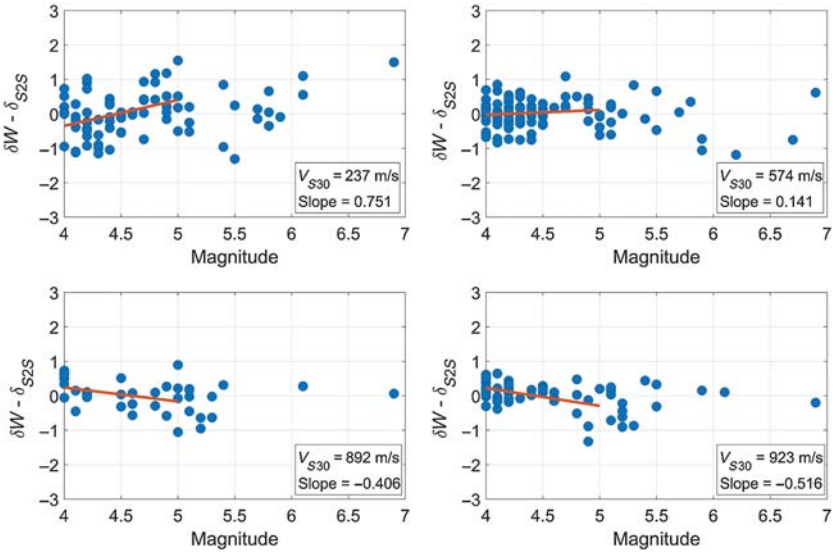

Figure 10. Within-event residuals (δW) corrected by the average site term for selected KiK-net stations. Values shown are for an oscillator period of 0.04. The V_{S30} of each station is shown, as well as the average slope for the event-corrected residuals for $M \leq 5$.

(δ_{S2S}). Observe that for the station with low V_{S30}, the magnitude dependence is positive and it becomes negative for the stations with higher V_{S30}. To explore whether this trend is systematic, we compute the slope of the magnitude dependence of the within-event residual for 118 stations with more than 30 recordings. Figure 11a shows the dependence of this slope on the average shear-wave velocity over the upper 30 m (V_{S30}), which can be considered a weak proxy for κ (Chandler *et al.*, 2006). There is a clear trend of positive magnitude dependence for stations with lower V_{S30}, and negative magnitude dependency for stations with high V_{S30}. Figure 11b plots the same data as a function of estimates of the zero-distance components of κ (i.e., κ_0) obtained for each station from Poggi *et al.* (2013). As expected, sites with lower κ_0 show more negative values of magnitude dependency. Recall that these trends are relative to the GMPE, and hence represent only relative magnitude dependency (relative to the average of all stations). Figure 11 validates the postulate that softer stations (i.e., with higher κ values) will show a stronger magnitude dependence than stiffer stations.

Implications

The findings discussed in the previous sections have a number of implications within engineering seismology and seismic hazard analysis. In this section, a number of these implications are discussed. It is not possible to provide a detailed investigation of each of these points within the scope of the current article, so the discussion in each case is deliberately left at a relatively high level.

Amplification Functions (Initiation of Nonlinearity)

The results summarized in Figures 7 and 8 demonstrated that for short-period spectral ordinates, the linear spectral amplification factors increase with increasing magnitude and increasing distance. In some cases, this feature may result in spectral amplification factors that possess attributes expected of nonlinear response despite being entirely linear, namely that the spectral amplification factors decrease as the intensity of the motion decreases. When developing functions to predict amplification as a function of reference motion amplitude, this apparent nonlinearity would typically be treated as though it was genuine nonlinearity. However, because the level of motion associated with these small-magnitude events is typically very low, it is possible to derive site amplification models that suggest that nonlinear behavior is occurring very early.

Nonlinear Amplification (Appearance of Nonlinearity)

Modern ground-motion models often include terms to account for nonlinear site response. These terms are frequently calibrated using numerical analyses because the effects of nonlinearity are not easily constrained directly from the data itself. In other cases, the general form of the nonlinear terms is developed on the basis of these numerical analyses but at least some of the actual model parameters are calibrated using the empirical data.

Figure 5 demonstrates an effect that poses a challenge to the calibration of nonlinear site-response terms. For short

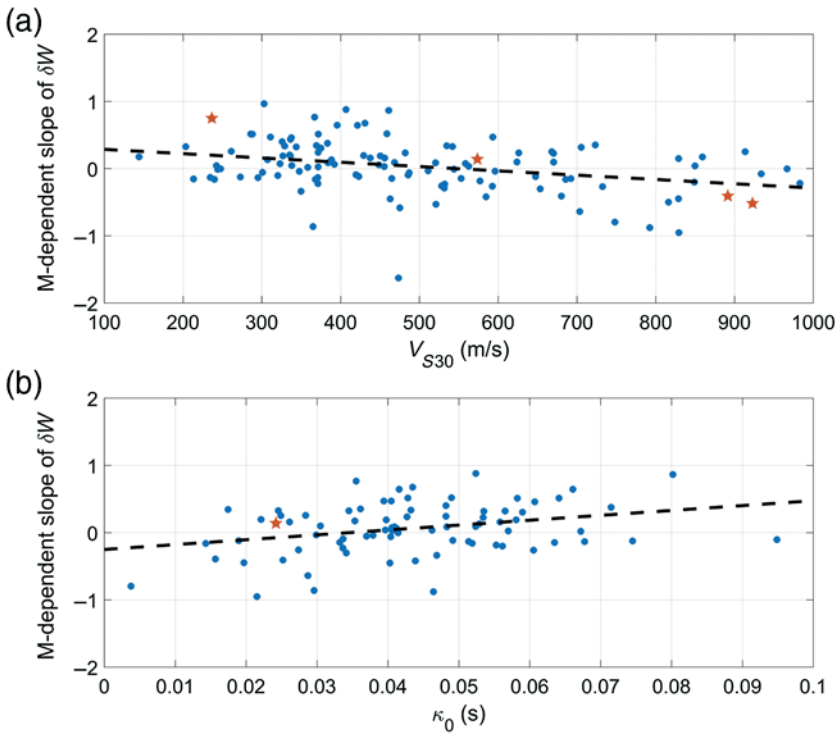

Figure 11. Slope of the within-event residuals for 118 KiK-net stations with at least 30 records. Red stars identify the stations shown in Figure 10. The dashed line corresponds to a linear fit to the data; (a) plotted versus V_{S30} and (b) plotted versus estimates of the site diminution parameter κ_0 (not all of the 118 stations had estimates of κ_0).

response periods, the figure indicates that the amplification for short-distance scenarios is significantly lower than that for the larger distances—precisely what would be predicted by nonlinear site response. The problem therefore becomes associated with decoupling the apparent nonlinearity associated with the magnitude and distance dependence of the linear site response with the actual nonlinearity associated with high levels of induced strain.

Site Terms for Single-Station Analysis

Site terms at single locations are currently estimated either through the use of random effects within a regression analysis or from decomposition of residuals given some ground-motion model and database. In all cases, these site terms are computed assuming that linear site response is independent of the scenario. Therefore, two sites with identical dynamic properties may appear to have very different site terms at short periods even when recording the same earthquakes as a result of the source-to-site distances being different for each event. Probably more significantly, it is assumed that the site term computed with small-magnitude data can be applicable to large magnitudes as well. The findings in this article show that this is not the case, hence considerable care must be taken when extrapolating site term estimates from small- to large-magnitude earthquakes when working in terms of response spectral ordinates. Similarly, if working with response spectral ordinates, estimates of site response obtained from small-magnitude data using the reference station method or downhole arrays cannot be readily extrapolated to larger magnitudes. To avoid extrapolation issues, direct estimates of site response (e.g., spectral ratios) should be computed in the Fourier domain, with application to response spectra through combination with the oscillator transfer function.

Magnitude-Dependent Variability

As discussed earlier, ground-motion models will be biased due to not considering the magnitude and distance dependence of the linear site response. Because this effect is most pronounced for the smaller earthquakes, the bias is also most pronounced for these events. These biases collectively contribute to the suggestion that the variance of spectral ordinates is magnitude dependent, and also at least partly explains why this magnitude dependence is more pronounced for the short-period ordinates. Evidence to this effect has been shown in Figure 9 for the site-to-site variability component (ϕ_{S2S}). Similarly, the magnitude dependence of the site term can explain the fact that the single-station phi (ϕ_{ss}) is generally larger for smaller magnitude earthquakes (Rodriguez-Marek *et al.*, 2013).

Convolution Approach to Soil Hazard

Bazzurro and Cornell (2004) presented a number of approaches to incorporate nonlinear site effects within probabilistic seismic hazard analysis. Of those discussed, the convolution approach is one that is commonly used to incorporate site-specific site-response effects into a hazard study. This approach to obtaining surface hazard curves from a hazard curve associated with some deeper velocity horizon implicitly assumes that site amplification effects are independent of the earthquake scenario.

The magnitude and distance dependence of the linear site effects discussed in this article provides a justification for incorporating the site-specific site-response terms directly within the hazard integral rather than via a convolution on the reference horizon hazard curve. In this way, the specific features of the site amplification that exist for each considered rupture scenario can be accounted for. However, depending upon the specific details of the study being undertaken, embedding the scenario dependence of the site response within the hazard integral may have significant implications in terms of computational demand. The key issue here relates to how epistemic uncertainties in site response are accounted for when a partially nonergodic approach is adopted.

Estimation of κ from Response Spectra

Studies such as those of Silva and Darragh (1995) and Silva *et al.* (1998) recognized that the values of κ could be inferred by finding the values of the parameter that resulted in the best match to short-period response spectral shape. More recently, these concepts have been used by Al Atik (2012) to outline a methodology whereby κ is directly estimated from the shape of response spectral at short periods. Often this assessment is made using records from relatively small-magnitude events where the level of site amplification will differ from that expected in large scenarios. As a result, the implied κ values that are obtained in this way are likely to be biased. This is another argument to support the use of Fourier spectral approaches to estimate κ over response spectral approaches.

However, care also needs to be taken if inferring Fourier spectral amplitudes from response spectra. Zandieh *et al.* (2016) recently observed that when using the inverse RVT approach (Al Atik *et al.*, 2014) to infer estimates of κ from the NGA-West2 ground-motion models, κ appears to be magnitude dependent. When viewed in the light of the present study, this apparent magnitude dependence of κ can be better understood as being an artifact of a scenario-independent linear site response. That is, the magnitude dependence of κ is required to compensate for the fact that the generic scenario-independent linear site response in the NGA-West2 models will typically overestimate the amplification at small magnitudes and underestimate amplification at larger magnitudes.

Conclusions

The primary conclusion of the article is that linear site spectral amplification factors depend upon the magnitude and distance of the causative scenario. The dependence is strong at short periods and is particularly pronounced for small-magnitude scenarios. This finding has significant implications for the way in which ground-motion models should be developed. When the scenario dependence of the linear site response is not explicitly considered, it will influence other components of the models. In particular, there is likely to be a direct impact on the magnitude scaling for relatively low magnitude scenarios. The quantification of nonlinear site-response terms may also be similarly impacted.

The theoretical considerations presented in this article have been clearly supported both by the numerical site-response calculations presented here as well as from direct observations of high-quality empirical data. The relatively simple concept of recognizing that near-surface layers are acting as an additional κ filter is not necessarily new. However, given that increased attention has been paid in recent years to extracting information from relatively small-magnitude events, understanding how this additional filter affects the frequencies contributing to response spectra allows us to successfully predict a number of issues of importance for engineering seismology. Many of these issues can be avoided using ground-motion models for response spectral ordinates that arise from combining FAS and duration prediction models (Bora *et al.*, 2015).

As noted throughout the article, the most significant evidence of the scenario dependence of linear site amplification manifests for small events, and findings from such events are often assumed appropriate for larger events. This is particularly the case when developing nonergodic or partially nonergodic ground-motion models for which the variance decompositions are normally dominated by small-magnitude data. Therefore, an important conclusion of the present article is that great care must be exercised when imposing constraints upon variance components of moderate-to-large magnitude events on the basis of analyses dominated by smaller events. Similarly, site terms estimated from small-magnitude events do not necessarily apply to larger magnitudes.

Data and Resources

Computations carried out for this research were undertaken using a combination of open-source Julia (http://julialang.org, last accessed September 2017) and MATLAB (www.mathworks.com/products/matlab, last accessed September 2017). Site profiles were used with permission from Nederlandse Aardolie Maatschappij (NAM). Details on these profiles were published in Kruiver *et al.* (2017) and are available on request. The KiK-net strong-motion data used in this study were provided by National Research Institute for Earth Science and Disaster Prevention (NIED) at www.kik.bosai.go.jp (last accessed September 2017, whereas the strong-motion data were last accessed in October 2012). The metadata that accompany the KiK-net ground-motion data were obtained from https://datacenterhub.org/resources/272 (last accessed September 2017).

Acknowledgments

The work presented in this article was prompted by engagement of the authors by Nederlandse Aardolie Maatschappij (NAM) to develop a ground-motion prediction and site-response model for the Groningen gas field in the Netherlands. The authors are grateful to NAM for permitting the use of the data and results from this project for this publication and to Jan van Elk for his leadership of the hazard and risk modeling project that has proven such a fertile ground for developing and disseminating new research. Partial funding for the work of the second author was provided by Electricité de France under cooperation Contract Number 3000-5910144023. The authors also wish to thank John Zhao and an anonymous reviewer for constructive feedback and comments on an earlier version of the article that helped to improve the final article. The authors particularly note Zhao's own work on the issue of magnitude and distance dependence of site amplification factors and are grateful for his insights and his positive appraisal of this article.

References

Abrahamson, N. A., W. J. Silva, and R. Kamai (2014). Summary of the ASK14 ground motion relation for active crustal regions, *Earthq. Spectra* **30,** no. 3, 1025–1055.

Al Atik, L. (2012). Kappa for candidate GMPEs, *SSHAC Level 3 Southwestern U.S. Ground Motion Characterization*, Workshop 1 presentation, Oakland, California, available at https://pge.com/includes/docs/pdfs/shared/edusafety/systemworks/dcpp/SSHAC/

sugmworkshops/Day3_am6_AlAtik-Kappa_from_CandidateGMPEs.pdf (last accessed September 2017).

Al Atik, L., A. Kottke, N. Abrahamson, and J. Hollenback (2014). Kappa (κ) scaling of ground-motion prediction equations using an inverse random vibration theory approach, *Bull. Seismol. Soc. Am.* **104,** no. 1, 336–346.

Anderson, J. G., and S. E. Hough (1984). A model for the shape of the Fourier amplitude spectrum of acceleration at high frequencies, *Bull. Seismol. Soc. Am.* **74,** no. 5, 1969–1993.

Bazzurro, P., and C. A. Cornell (2004). Nonlinear soil-site effects in probabilistic seismic hazard analysis, *Bull. Seismol. Soc. Am.* **94,** no. 6, 2110–2123.

Bommer, J. J., P. J. Stafford, B. Edwards, B. Dost, E. van Dedem, A. Rodriguez-Marek, P. Kruiver, J. van Elk, D. Doornhof, and M. Ntinalexis (2017). Framework for a ground-motion model for induced seismic hazard and risk analysis in the Groningen gas field, The Netherlands, *Earthq. Spectra* **33,** no. 2, 481–498.

Boore, D. M. (2003). Simulation of ground motion using the stochastic method, *Pure Appl. Geophys.* **160,** no. 3, 635–676.

Boore, D. M., and K. W. Campbell (2017). Adjusting central and eastern North America ground-motion intensity measures between sites with different reference-rock site conditions, *Bull. Seismol. Soc. Am.* **107,** no. 1, doi: 10.1785/0120160208.

Bora, S. S., F. Scherbaum, N. Kuehn, and P. J. Stafford (2016). On the relationship between Fourier and response spectra: Implications for the adjustment of empirical ground-motion prediction equations (GMPEs), *Bull. Seismol. Soc. Am.* **106,** no. 3, 1235–1253.

Bora, S. S., F. Scherbaum, N. Kuehn, P. J. Stafford, and B. Edwards (2015). Development of a response spectral ground-motion prediction equation (GMPE) for seismic-hazard analysis from empirical Fourier spectral and duration models, *Bull. Seismol. Soc. Am.* **105,** 2192–2218.

Bozorgnia, Y., N. A. Abrahamson, L. Al-Atik, T. D. Ancheta, G. M. Atkinson, J. W. Baker, A. Baltay, D. M. Boore, K. W. Campbell, B. S.-J. Chiou, *et al.* (2014). NGA-West2 research project, *Earthq. Spectra* **30,** no. 3, 973–987.

Brune, J. N. (1970). Tectonic stress and the spectra of seismic shear waves from earthquakes, *J. Geophys. Res.* **75,** no. 26, 4997–5009.

Campbell, K. W. (2009). Estimates of shear-wave Q and kappa(0) for unconsolidated and semi-consolidated sediments in eastern North America, *Bull. Seismol. Soc. Am.* **99,** 2365–2392.

Chandler, A. M., N. T. K. Lam, and H. H. Tsang (2006). Near-surface attenuation modelling based on rock shear-wave velocity profile, *Soil Dynam. Earthq. Eng.* **26,** no. 11, 1004–1014.

Chiou, B., R. R. Youngs, N. A. Abrahamson, and K. Addo (2010). Ground-motion attenuation model for small-to-moderate shallow crustal earthquakes in California and its implications on regionalization of ground-motion prediction models, *Earthq. Spectra* **26,** no. 4, 907–926.

Darendeli, M. (2001). Development of a new family of normalized modulus reduction and material damping curves, *Ph.D. Thesis*, Department of Civil Engineering, University of Texas, Austin, Texas.

Dawood, H. M. (2014). Partitioning uncertainty for non-ergodic probabilistic seismic hazard analyses, *Ph.D. Thesis*, Department of Civil & Environmental Engineering, Virginia Polytechnic Institute and State University, Blacksburg, Virginia.

Dawood, H. M., A. Rodriguez-Marek, J. Bayless, C. Goulet, and E. Thompson (2016). A flatfile for the KiK-net database processed using an automated protocol, *Earthq. Spectra* **32,** no. 2, 1281–1302.

Hough, S. E., and J. G. Anderson (1988). High-frequency spectra observed at Anza, California: Implications for Q structure, *Bull. Seismol. Soc. Am.* **78,** no. 2, 692–707

Kottke, A. R., and E. M. Rathje (2008). Technical manual for Strata, *PEER Report 2008/10*, Pacific Earthquake Engineering Research Center, University of California, Berkeley, 100 p.

Kruiver, P. P., E. van Dedem, R. Romijn, G. L. de Lange, M. Korff, J. Stafleu, A. Rodriguez-Marek, J. J. Bommer, J. van Elk, and D. Doornhof (2017). An integrated shear-wave velocity model for the Groningen gas field, The Netherlands, *Bull. Earthq. Eng.* **15,** no. 9, 3555–3580.

Menq, F. Y. (2003). Dynamic properties of sandy and gravelly soils, *Ph.D. Thesis*, Department of Civil Engineering, University of Texas, Austin, Texas.

Poggi, V. B., B. Edwards, and D. Fäh (2013). Reference S-wave velocity profile and attenuation models for ground-motion prediction equations: Application to Japan, *Bull. Seismol. Soc. Am.* **103,** 2645–2656.

Rodriguez-Marek, A., F. Cotton, N. A. Abrahamson, S. Akkar, L. Al Atik, B. Edwards, G. A. Montalva, and H. M. Dawood (2013). A model for single-station standard deviation using data from various tectonic regions, *Bull. Seismol. Soc. Am.* **103,** no. 6, 3149–3163.

Silva, W. J., and R. Darragh (1995). Engineering characterization of earthquake strong ground motion recorded at rock sites, *Electric Power Research Institute, Palo Alto, Report Number TR-102261*.

Silva, W. J., R. Darragh, N. Gregor, G. Martin, N. Abrahamson, and C. Kircher (1998). Reassessment of site coefficients and near-fault factors for building code provisions, *Technical Report Program Element II: 98-HQGR-1010*, Pacific Engineering and Analysis, El Cerrito, California.

Zandieh, A., K. W. Campbell, and S. Pezeshk (2016). Estimation of implied by the high-frequency shape of the NGA-West2 ground-motion prediction equations, *Bull. Seismol. Soc. Am.* **106,** no. 3, 1342–1356.

Zhang, J., and J. X. Zhao (2009). Response spectral amplification ratios from 1- and 2-dimensional nonlinear soil site models, *Soil Dynam. Earthq. Eng.* **29,** 563–573.

Zhao, J. X., J. S. Hu, F. Jiang, J. Zhou, and D. A. Rhoades (2015). Nonlinear site models derived from 1-D analyses for ground-motion prediction equations using site classes as the site parameter, *Bull. Seismol. Soc. Am.* **105,** no. 4, 2010–2022.

Zhao, J. X., J. Zhang, and K. Irikura (2009). Side-effect of using response spectral amplification ratios for soil sites—Variability and earthquake-magnitude and source-distance dependent amplification ratios for soil sites, *Soil Dynam. Earthq. Eng.* **29,** 1262–1273.

Department of Civil & Environmental Engineering
Imperial College London
London SW7 2AZ, United Kingdom
p.stafford@imperial.ac.uk
(P.J.S., J.J.B.)

The Charles E. Via, Jr. Dept of Civil & Environmental Engineering
Virginia Tech
Blacksburg, Virginia 24061
(A.R.-M.)

Department of Earth, Ocean and Ecological Sciences
University of Liverpool
Liverpool L69 3GP, United Kingdom
(B.E.)

Deltares
P.O. Box 85467
3508 AL Utrecht, The Netherlands
(P.P.K.)

Manuscript received 13 March 2017;
Published Online 17 October 2017